Journal of Solid State Electrochemistry
https://doi.org/10.1007/s10008-024-06084-1

ORIGINAL PAPER

Contribution of Ti insertion on nano-crystalline rich oxygen vacancy V_2O_5's performance for supercapacitor electrodes

Khaled Faisal Qasim[1] · Samar Abdel-Hamied[2] · M. M. El-Desoky[3]

Received: 23 April 2024 / Revised: 21 August 2024 / Accepted: 9 September 2024
© The Author(s), under exclusive licence to Springer-Verlag GmbH Germany, part of Springer Nature 2024

Abstract

The sol–gel film method was employed to produce pure and Ti-doped V_2O_5 in varying concentrations (1, 2, 3, and 4 mol%). The resulting materials were characterized using X-ray diffraction (XRD), scanning electron microscopy with energy dispersive X-ray spectroscopy (SEM–EDX), transmission electron microscopy (TEM), Brunauer–Emmett–Teller (BET) surface area analysis, and X-ray photoelectron spectroscopy (XPS) to assess their crystal structure, morphology, surface characteristics, and elemental composition. XRD results indicated that all samples, whether pure or doped, crystallized in the orthorhombic phase with a preferred orientation along the (101) plane. The introduction of doping reduced the crystallite size, which fell below 10 nm. SEM analysis revealed that the V_2O_5 appeared as nanosheets. The impact of doping on electrochemical performance was evaluated using galvanostatic charge/discharge (GCD), electrochemical impedance spectroscopy (EIS), and cyclic voltammetry (CV) in a 1 M $LiNO_3$ electrolyte. The electrochemical tests demonstrated surface redox pseudocapacitive behavior with reversible charge/discharge capabilities, and specific capacitance values ranged from 254.6 to 352.3 F/g, depending on the sample composition, as determined by CV. The presence of dopants enhanced the electrochemical performance due to the multiple oxidation states of V and Ti, as well as the presence of oxygen vacancies ($V_O^{\cdot\cdot}$). Specifically, the 4% Ti-doped V_2O_5 exhibited a specific capacitance (C_{sp}) of 352.3 F/g, energy density (E_d) of 43.3 Wh/kg, power density (P_d) of 554.2 W/kg, and maintained 69.1% cycling stability over 10,000 cycles at 1 A/g.

Keywords Sol–gel films · Nanostructure · XRD · Supercapacitor · Energy storage

Introduction

Renewable energy storage has been universally used in the modernized world, such as in portable electronics, electric vehicles, and grid-scale energy storage. In the current technologies, as far as energy storage is involved, asymmetric hybrid supercapacitors have acquired considerable momentum due to their working potential and energy density [1]. Transition metal oxides (TMO) have attracted the interest of researchers as potential supercapacitor electrode materials [2].

Metal oxides' remarkable stability and electrochemical characteristics make them essential to the development of supercapacitors. These substances, which include cobalt oxide (Co_3O_4), manganese oxide (MnO_2), and ruthenium oxide (RuO_2), are prized for their extended cycle life, high specific capacitance, and superior charge/discharge efficiency [3]. The energy and power density of supercapacitors are greatly increased by the reversible electrochemical reactions that metal oxides can undergo due to their redox-active nature. To further enhance performance, metal oxides frequently have large surface areas and excellent electrical conductivity, which enable quick ion and electron movement. Reliable operation over long periods of time is ensured by their capacity to retain structural integrity and stability under heavy charge/discharge cycles [4, 5]. Metal oxides are therefore essential to the advancement of supercapacitor technology for a range of applications, like energy storage

✉ Khaled Faisal Qasim
khaled.faisal@fsc.suezuni.edu.eg;
khaled_faisal92@hotmail.com

✉ M. M. El-Desoky
mmdesoky@suezuniv.edu.eg; mmdesoky@gmail.com

[1] Chemistry Department, Faculty of Science, Suez University, Suez 43518, Egypt

[2] Basic Science Department, Faculty of Engineering at Shoubra, Benha University, Benha, Egypt

[3] Physics Department, Faculty of Science, Suez University, Suez 43518, Egypt

Published online: 04 October 2024

systems in electric vehicles, renewable energy integration, and portable electronic devices [6].

Vanadium is a transition metal component that naturally occurs as a mineral. Vanadium is less costly, greener, and less polluting than cobalt, ruthenium, and manganese. Vanadium is a multivalent metal compound because it includes five valence electrons in the uppermost layer of the element [7]. V^{5+} is the most stable, followed by V^{4+}, and V^{3+} and V^{2+} are among the least durable. As a result, many studies have been done on V_2O_5, VO_2, and V_6O_{13} [8]. V_2O_5 is well recognized for its distinct layered structure and unique properties in electronics, optics, and electrochemistry. Additionally, it's cheap, has simple synthesis, and has a range of chemical valence states. As a result, it is extensively used in lithium-ion batteries, smart material devices, sensors, capacitors, and catalysts [9].

The V_2O_5 crystals possess an orthorhombic structure with lattice constants of a = 11.15 Å, b = 3.56 Å, and c = 4.37 Å [10]. The distorted V_2O_5 structure depends on where the V in V_2O_5 is located. The 3 different shapes of the 5 (O) atoms allow the VO_4 tetrahedral unit to be joined into a chain by the oxygen bridge. The 5th oxygen atom in a chain connects the two chains, creating a layered structure. The oxygen atoms in the other layer are then linked to those in the 1st layer, and 6 O atoms surround each vanadium atom. The distorted octahedron formed by the 0.28 nm layer gap eventually gives rise to a V_2O_5 crystal [11].

In the 1960s, Tompkins proposed the idea of oxygen vacancy, regarded as a material in solid surface chemistry. The absence of oxygen atoms from the metallic oxide lattice, which also occurs in composites containing oxygen, results in oxygen vacancies ($V_O^{\cdot\cdot}$). This kind of hole will lead to crystal flaws and hasten the formation of holes in the lattice. This resulted in many oxygen vacancies in metal oxides, thus expanding the spectrum of potential uses for these materials [12–14].

Studies have shown that V_2O_5 includes many thermally activated polarons that can serve as carriers for the intrinsic n-type semiconductor V_2O_5 due to the high ratio of ($V_O^{\cdot\cdot}$) during the high-temperature synthesis [9]. As a result, O^{-2} ions overflow brought by defects will be more agreeable to doping, significantly increasing ion transport efficiency in the electrochemical process [15].

However, the V_2O_5 electrode material has poor cycling performance and tiny capacitance due to the intrinsically low conductivity and slow charge diffusion in the cycling process, which limits its practical application. Numerous techniques have been created to address this issue and enhance the electrochemical performance of V_2O_5 [7]. For instance, the V_2O_5 nanostructures' size and shape can be optimized through the composition and assembly process of V_2O_5 electrode nanostructures, which can successfully boost the mass and charge transfer of the electrode materials in the charge–discharge process and adapt to the volume change in the cycle process [11, 16].

For instance, Li et al. [17] found that the outstanding electrochemical performance was due to the ultrathin nanoplate shape and sulfide concentration. Finally, research has been done on the V_2O_5 nanomaterial for supercapacitors with various morphologies, including nanowires, nanosheets, and nanospheres Zhu et al. [18] disclosed V_2O_5 nanosheet arrays with a specific capacitance of 451 F/g. Many researchers attempt to create composite materials using V_2O_5 electrodes, carbon nanotubes, graphene, or conductive polymers in addition to designing their morphology and structure, to enhance the conductivity and chemical performance of the electrode/electrolyte interface [19].

To create the higher-performing supercapacitor electrode (capacitance is up to 618 F/g), Bi et al. [20] combined V_2O_5 nanofilms with a variety of conductive polymers. Additionally, the surface crystal structure of V_2O_5 electrode materials can be altered using flaws. Because of the high concentration of oxygen vacancies during the high-temperature V_2O_5 synthesis, studies have demonstrated that the sample contains a significant amount of thermally activated polarons that can serve as carriers for the intrinsic n-type semiconductor V_2O_5. Defect-induced oxygen ion overflow will therefore be more conducive to ion doping and adsorption, which will significantly increase the efficiency of ions being transported during the electrochemical reaction [15, 21].

V_2O_5 can be used for smart materials as electrochromic material owing to its varied oxidation states with different colors. Salek et al. [22] prepared Ti-doped V_2O_5 from a polyol process is reported. A high Ti concentration (up to 8.5 mol % of the total metallic content) can be inserted in vanadium oxide thanks to the synthesis route leading to nanometric crystallites as electrochromic materials. Films elaborated from a dip-coating process from oxide particle suspensions exhibited three distinct colorations during the redox cycling in lithium-based electrolytes. These colors were associated with three distinct oxidation states for the vanadium ions: + III (blue), + IV (green), and + V (orange). The morphology of the films was shown to drastically impact the electrochromic performances in terms of electrochemical capacity and stability.

In light of the discussions above, improving the electrochemical performance of V_2O_5-based electrodes for supercapacitors is still essential. The results of this study make it clear that $V_O^{\cdot\cdot}$ vacancy, a particular type of lattice defect, can control the electronic structure of transition metal oxides while maintaining the lattice's general invariance [17, 23]. This has a significant positive impact on the transition metal oxides' electrochemical properties [12, 24]. Additionally, oxygen vacancies can improve charge transmission in electrode materials even when there are several layers between them and keep the electrode materials' structural integrity

during the electrochemical process. Therefore, the electrode's capacitance can be improved, and cycle times can be extended by introducing $V_O^{\cdot\cdot}$ vacancies into transition metal oxides [25, 26].

In this study, we use sol–gel film method for preparation of pure and Ti-doped V_2O_5 in varying concentrations (1, 2, 3, and 4 mol%), which create oxygen vacancies. Hence, it increases the capacitive behaviour for supercapcitor applications.

Experimental

Preparation of x%Ti-V_2O_5

Titanium dioxide (TiO_2), vanadium pentoxide (V_2O_5) powder, and H_2O_2 were purchased from Sigma Aldrich with 99.9% purity. Based on the used procedure before [27]. The gelation was not forming in 5 different samples of x%TiO_2-V_2O_5, where x = 0, 1, 2, 3, and 4 mol% as exceeding the TiO_2 content to more than 4.0 mol%. Then, for each concentration, the doping weights of TiO_2 and V_2O_5 are prepared and added to 30 ml of 25% H_2O_2 with vigorous stirring to obtain a homogenous mixture. A thermal reaction starts and the mixture cools down while stirring, forming a gel. After the gel forms, we get the powder after leaving it in the air at room temperature for 2 weeks.

Materials characterizations and measurements

Cu-K with $\lambda = 0.154$ nm and a diffraction angle between 15° and 80° was used in an X-ray diffractometer (Philips XL 40) to record the XRD patterns of the materials. The morphology of the materials and surface elemental analysis were analyzed with a scanning electron microscope (SEM/EDX/EDX mapping) (JEOL-JSM-6510 LV). X-ray photoelectron spectroscopy (XPS) studies were performed using a KRATOS XSAM-800 and calibrated by adventitious carbon.

Cyclic voltammetry (CV) and galvanostatic charge–discharge (GCD) techniques were used using the Digi-Ivy 2116 B instrument to determine the studied electrodes' energy storage capacity. EIS was measured by (Metrohm Auto Lab (PGSTAT 204), Netherlands, between 0.1 Hz and 100 kHz at a constant voltage of 20 mV. A cell with three electrodes was used to determine the electrochemical characteristics. The Ag/AgCl electrode and Pt foil served as reference and counter electrodes, respectively. CVs were run between -0.3 and 0.7 V at scan rates between 5 and 100 mV/s. GCD was measured between 0.5 and 3 A/g of current density in 1 M $LiNO_3$ aqueous solution. For electrode preparation, V_2O_5 samples, carbon black, and polyvinylidene fluoride in the weight proportions of 80:10:10 were suspended in DMF to make a paste of mixture, then substrated on FTO glass and left to dry at 200 °C for 2 h to get the best adhesion of samples on the surface of FTO.

Results and discussions

Characterizations

Figure 1 shows the XRD patterns of the pure and doped V_2O_5 samples. The diffraction peaks for V_2O_5 are at $2\theta = 12.4°$, 23.5°, 25.4°, 26.5°, 30.7°, 34.5°, 38.6°, 47°, 50.5°, and 60.5°, corresponding to (200), (101), (110), (201), (301), (310), (401), (501), (020), (420) planes, respectively. They correspond to the V_2O_5 orthorhombic phase structure (JCPDS card no. 41–1426) [28]. The same peaks were also seen in the XRD of the doped V_2O_5. Additionally, it was noted that introducing dopant Ti ion into the V_2O_5 made the (101) crystal plane move noticeably to the left. This shift is due to the presence of atoms with smaller substituted ionic radii (the ionic radius of V^{5+} is 46 pm, which is smaller than $Ti.^{4+}$ 60 pm) [29, 30]. These results suggest that the dopant was effectively generated in the (101) plane of the V_2O_5 lattice. It's noticed that Ti dopant increases lead to a decrease in the intensity of (101) for the plane (110), which means that the Ti dopants are oriented on the plane (101). In conclusion, The XRD results confirm no modification in the structure but a change in lattice parameters as V_2O_5 exhibits orthorhombic structure with space group (Pmmn2), the lattice constant (a), (b), and (c) is computed by using lattice space d_{hkl} using Eq. (1) [31]

$$d_{hkl} = \sqrt{\frac{a^2}{h^2} + \frac{b^2}{k^2} + \frac{c^2}{l^2}} \tag{1}$$

The results obtained are also listed in Table 1, which shows an increase in the (a) lattice parameter, a decrease in the (c) lattice parameter, and the constancy of (b) of all doped materials. This substitution can promote the reduction of Ti^{4+} to Ti^{3+} to balance the charge [32]. This may be the reason for the change in the lattice constant parameter of the V_2O_5 specimen because the ionic radius of Ti^{3+} (67 pm) is larger than that of Ti^{4+} (60 pm) [30]. Those results were compared with data refined using Rietveld refinement and listed in Table 1.

The average crystallite size of V_2O_5 samples was calculated using Scherrer-Debye Eq. (2) [31]

$$D = \frac{0.9\ \lambda}{\beta \cos\theta} \tag{2}$$

where λ is the X-ray wavelength employed, and β denotes (FWHM). The results are also reported in Table 1, illustrating that all the samples lie on the nanometer scale. Their

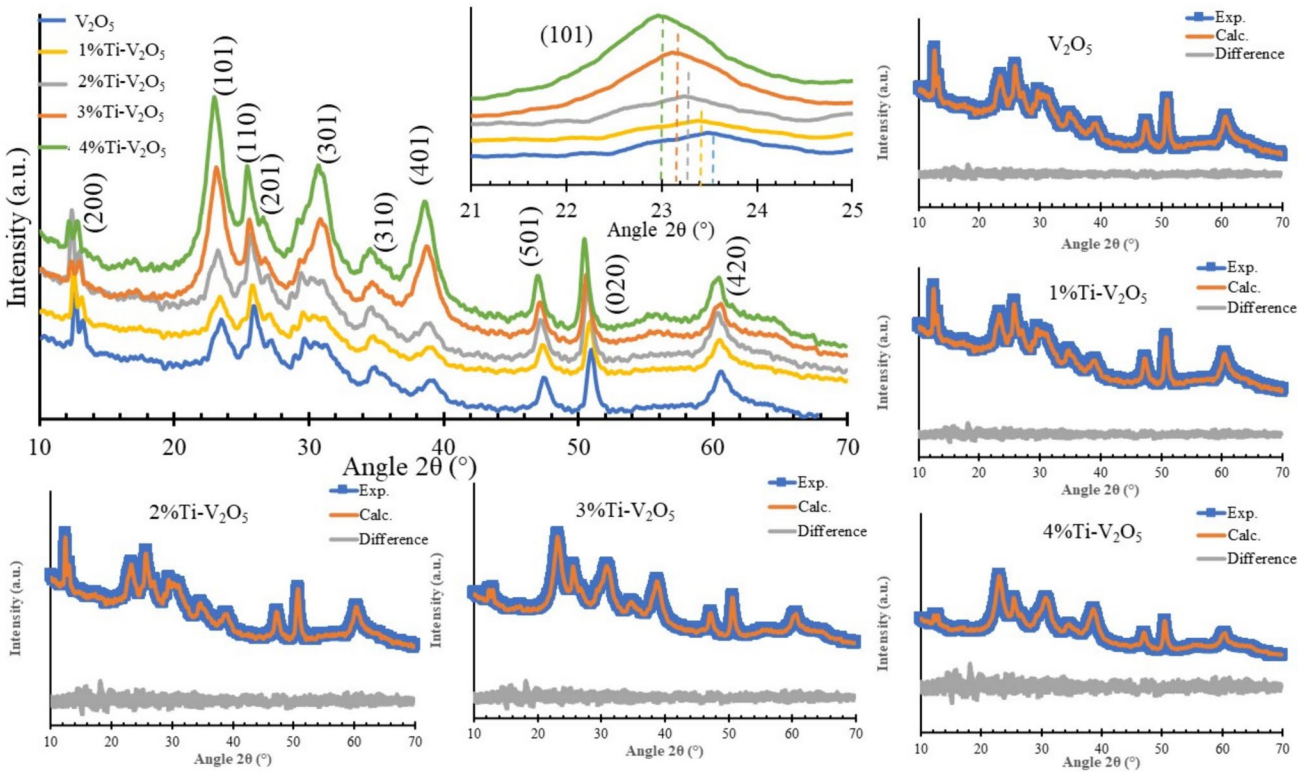

Fig. 1 XRD and refinment of the prepared samples

Table 1 XRD and surface data of pure and doped V_2O_5 samples

Sample	SSA (m^2/g)	V_r (nm)	Scherer Debye			Lattice Parameter				Refinement			
			D (nm)	δ (line/m^2)	ε ($\times 10^{-3}$)	a (Å)	b (Å)	c (Å)	V (Å^3)	a (Å)	b (Å)	c (Å)	V (Å^3)
V_2O_5	5.3	4.53	9.7 ± 0.12	8.12×10^{15}	2.56	11.94	3.56	4.12	175.12	11.85	3.516	4.05	168.7
1%Ti-V_2O_5	6.5	4.24	9.2 ± 0.09	1.02×10^{16}	2.94	11.51	3.56	4.36	178.65	11.61	3.547	4.37	179.9
2%Ti-V_2O_5	7.4	3.94	8.0 ± 0.12	1.57×10^{16}	4.36	10.35	3.56	4.91	180.91	10.33	3.597	4.82	179.0
3%Ti-V_2O_5	9.1	3.87	7.2 ± 0.08	8.31×10^{15}	4.62	9.81	3.57	5.28	184.91	9.95	3.627	5.31	191.6
4%Ti-V_2O_5	11.5	3.79	6.8 ± 0.08	2.28×10^{16}	5.86	9.72	3.58	5.34	185.81	9.83	3.635	5.37	191.8

sizes drop when a dopant is added due to the difference in their ionic radii with the ionic radius of Ti [33].

The strain (ε) induced in the samples was calculated using Eqs. (3) and (4) [34]

$$\beta_s = 4\varepsilon \tan \theta \tag{3}$$

$$\varepsilon = \frac{\beta \cos\theta}{4} \tag{4}$$

The results are listed in Tables 1 and 2, which show an increase in the strain of pure V_2O_5 due to the addition of the dopant ratio. This can be explained because the ionic radii of V ions are smaller than Ti [35]. Therefore, the replacement of V^{5+} ions by Ti^{4+} will lead to an increase in ε of V_2O_5 crystals [36]. The addition of dopants increases ε due to the shrinkage of the Lattice constant compared with pure V_2O_5.

The dislocation density (ρ_D), which is defined as the length of the dislocation line per unit volume of the crystals, is calculated by using Eqs. (5) and (6) [37]

$$\rho_D = \frac{1}{D^2} \tag{5}$$

$$\rho_D = \frac{15\varepsilon}{aD} \tag{6}$$

Table 2 XRD data of samples using Williamson-Hall (W–H) functions

Sample	Williamson-Hall (Eq. 9)			Williamson-Hall (Eq. 10)		
	D (nm)	δ (line/m^2)	ε ($\times 10^{-3}$)	D (nm)	δ (line/m^2)	ε ($\times 10^{-3}$)
V_2O_5	10.3 ± 0.01	8.19×10^{15}	2.88	13.3 ± 0.007	5.6×10^{15}	2.56
1%Ti-V_2O_5	9.8 ± 0.012	1.06×10^{16}	3.58	12 ± 0.011	6.88×10^{15}	2.94
2%Ti-V_2O_5	8.6 ± 0.009	1.64×10^{16}	4.42	11.2 ± 0.013	7.9×10^{15}	4.36
3%Ti-V_2O_5	7.9 ± 0.007	2.07×10^{16}	5.69	9.2 ± 0.009	1.17×10^{16}	4.62
4%Ti-V_2O_5	7.4 ± 0.008	2.35×10^{16}	6.13	8.5 ± 0.01	1.4×10^{16}	5.86

The results obtained are given in Tables 1 and 2), which shows that adding dopants leads to an increment in ρ_D value due to the dissimilarity of either ionic radii or valence charges between the substituted dopant and the host element. That increases the bulk deformation of crystals [36].

The following analysis assumes that the diffraction line widening due to crystallite size (β_D) and crystal microstrain (β_s) are additive quantities [30].

$$\beta_{hkl} = \beta_s + \beta_D \tag{7}$$

From Eq. (3, 4), it leads to the following relationship:

$$\beta_{hkl} = \frac{K\lambda}{D_{XRD}\ cos\,\theta} + 4\ \varepsilon\ \tan\ \theta \tag{8}$$

Rearranging Eq. (8), we obtain:

$$\beta_{hkl}\ \cos\ \theta = \frac{K\lambda}{D_{XRD}} + 4\varepsilon \sin\theta \tag{9}$$

The outcomes are listed in Table 2, which demonstrates that doped V_2O_5 samples have lower particle sizes than the pure ones. In the process, $V_O^{\cdot\cdot}$ vacancy causes defects and partial amorphization, resulting in a reduction in crystallite size [38]. It is apparent that the (ε) and (ρ_D) for doped V_2O_5 samples increase with dopant insertion due to the reduction in particle sizes [39].

Parameters of the W–H plots, as shown in Fig. 2, can be achieved by using averaged plots, which give less weight to reflections at high 2θ, where accuracy is often poorer. This approximation assumes a Lorentzian function for the crystallite size profile and a Gaussian function for the strain profile [40]. As a result, we have:

$$(d_{hkl}\beta_{hkl}\cos\ \theta)^2 = \frac{K\lambda}{D_{XRD}}\left(d^2{}_{hkl}\beta_{hkl}\cos\ \theta\right) + \left(\frac{\varepsilon}{2}\right)^2 \tag{10}$$

K is a constant hanging on the particle shape; for spherical particles, K" = 3/4. In Fig. 1, the term $(d_{hkl}\beta_{hkl}\ \cos\ \theta)^2$ is plotted as a function of $d^2{}_{hkl}\beta_{hkl}\ \cos\ \theta$ for all orientations of V_2O_5 samples, Results of the W–H and size-strain are shown in Fig. 2 and listed in Table 2.

Figure 3 shows SEM images of V_2O_5 samples. Uniformly dispersed V_2O_5 nanoparticles are seen in layered forms. The grain sizes of V_2O_5 samples are observed to be in the order of ~ 10 µm to ~ 40 µm. This morphology enhances the surface that would aid the double-layer capacitance of the charge from the electrolyte into the bulk of the V_2O_5.

The EDX and EDX mapping spectra in Fig. 4 confirm the elements present in the V_2O_5 doped samples to be V, O, and Ti. The surface maps show the uniform distribution of elements in the V_2O_5 nanosheet. The surface elemental analysis (atomic %) from EDX is listed in Table 3.

The TEM was also analyzed for V_2O_5 samples using different magnifications to elucidate the sheet structure obtained as shown in Fig. 5. Addition of Ti dopant doesn't affect the main morphology of V_2O_5 with a varied range in the nanoscale.

The electrochemical performance, as shown later, demonstrated that doped samples of V_2O_5 show better behaviors than pure ones due to the types of bonds and variations of valence states in doped samples, which can be analyzed using the XPS technique. The surface elemental analysis (atomic %) from XPS is listed in Table 3. As shown in Fig. 6 a,b, c are for 4% Ti-V_2O_5 and d,e are for pure V_2O_5, the main elements are V, O, and Ti. V ($2p^{1/2}$) spectrum shows three peaks with binding energies of 516.1 and 517.1 eV for V^{+4} and V^{+5}. A slight shift has appeared in doped samples at 514.8, 516.1, and 517.1 eV, which are related to V^{+3}, V^{+4}, and V^{+5}, respectively [41–45] and refer to the presence of various oxidation states of V ions. The absence of V^{3+} ion may rely on the lack of Ti dopant. O(1s) in pure V_2O_5 shows peaks at 530.1 eV, 530.6, and 531.9 eV related to V–O, $V_O^{\cdot\cdot}$ vacancy [46, 47], and H_2O, respectively [42, 48, 49]. The doped sample shows a slight deviation for the same peaks from the pure V_2O_5 at 529.6, 530.5, and 532 eV related to V–O, $V_O^{\cdot\cdot}$ vacancy [50], and H_2O, respectively. It's observed that the $V_O^{\cdot\cdot}$ vacancy ratio increased with doping addition due to variation in ionic radius between Ti^{4+} and V^{5+}. It's also confirmed by the presence of V^{4+} and V^{3+} reflecting the oxygen vacancy in the V_2O_5 [51, 52]. Ti ($2p^{3/2}$) bands observed at 458.1 eV and 458.6 eV are assigned for Ti^{+3}, and Ti^{+4} ($2p^{1/2}$), respectively [48].

For further assumed consideration of surface parameters, N_2 adsorption–desorption isotherms are studied

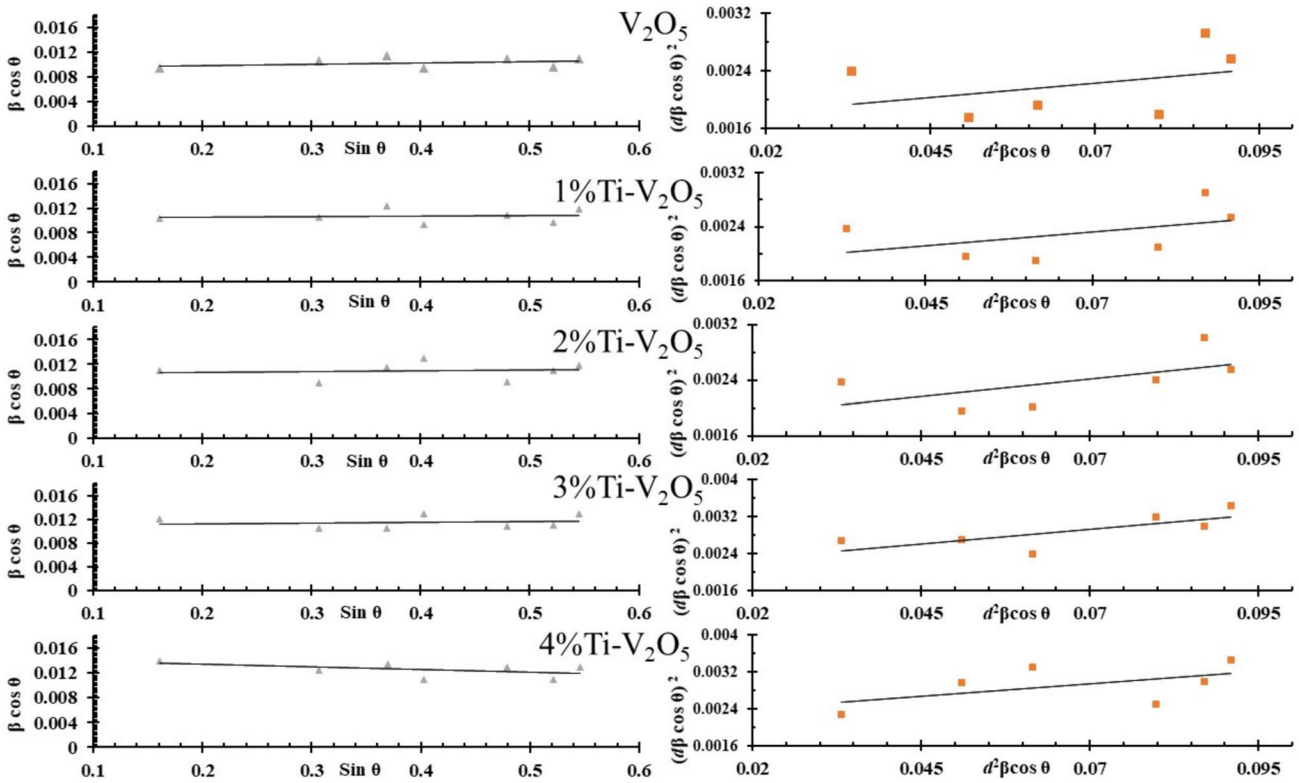

Fig. 2 W–H plots of the prepared samples

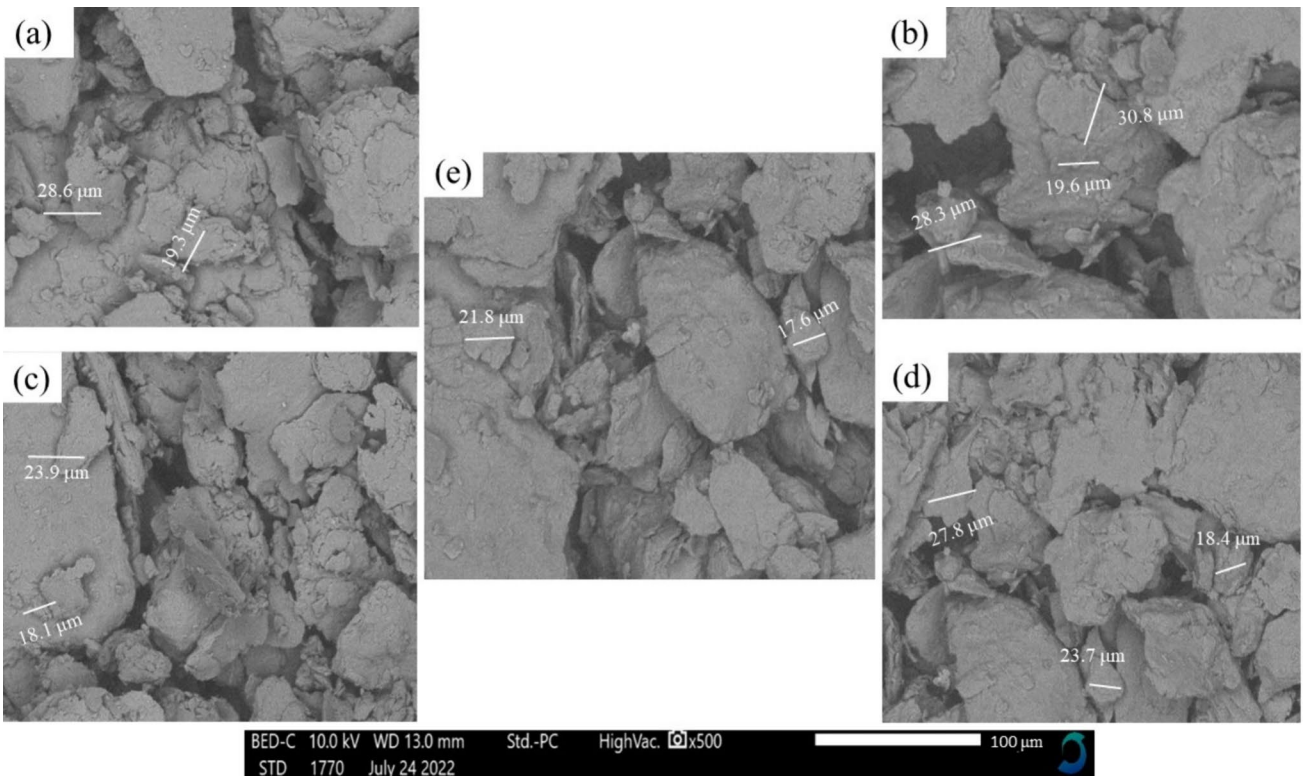

Fig. 3 SEM of **a**) pure, **b**) 1%, **c**) 2%, **d**) 3%, e) 4% Ti-doped V_2O_5

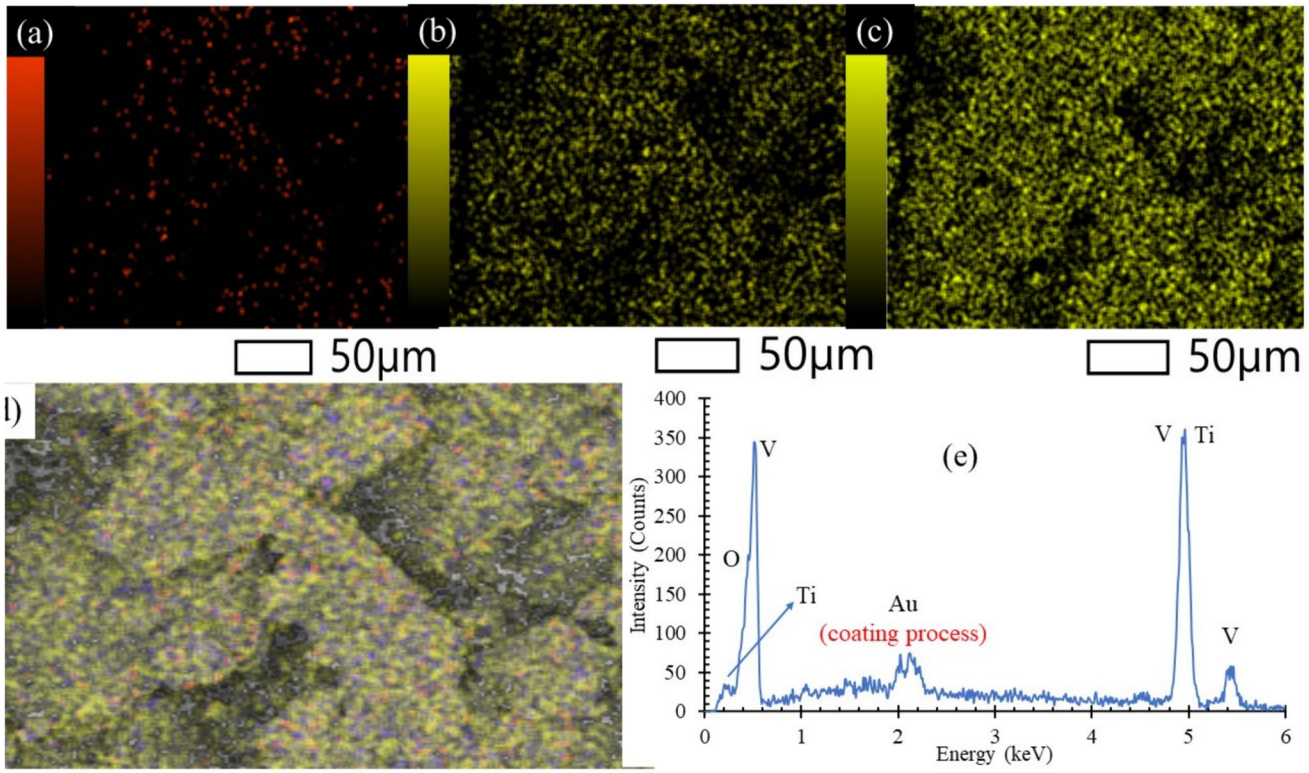

Fig. 4 EDX mapping of **a**) Ti, **b**) O, **c**) V, **d**) all elements, **e**) EDX of doped V_2O_5

Table 3 Elemental ratio of the prepared materials

Sample	SEM–EDX (Atomic %)			XPS (Atomic %)		
	V	O	Ti	V	O	Ti
V_2O_5	48.6 ± 1.9	51.4 ± 2.1	—	51.1 ± 1.4	48.9 ± 1.6	—
1%Ti-V_2O_5	47.3 ± 1.9	51.9 ± 2.1	0.7 ± 0.3	47.2 ± 1.4	52.3 ± 1.8	0.5 ± 0.2
2%Ti-V_2O_5	47 ± 3.1	51.3 ± 1.9	1.3 ± 0.4	46.4 ± 2.4	52.1 ± 2.1	1.4 ± 0.3
3%Ti-V_2O_5	46 ± 3.5	50.5 ± 1.5	2.5 ± 0.5	45.6 ± 3	50.5 ± 1.4	2.2 ± 0.3
4%Ti-V_2O_5	46 ± 3.8	50.5 ± 1.8	3.4 ± 0.7	44.4 ± 3.1	51.1 ± 1.7	3.4 ± 0.7

and revealed in Fig. 7. The isotherms of V_2O_5 samples are classified as a typical type IV [53], which shows the mesoporous nature of the materials. The addition of dopant doesn't change the isotherm type, but variation happened in surface parameters like specific surface area (SSA) and pore volume (V_p). Surface parameters are listed in Table 1.

Electrochemical studies

To understand the storage mechanism and parameters, some electrochemical techniques should be performed to evaluate the material's ability and whether it can be used for energy storage applications. The electrochemical behavior of pure and doped V_2O_5 is displayed in Figs. 8, 9 and 10.

The galvanostatic charge–discharge (GCD) method was also used to investigate the electrodes' electrochemical behavior at a constant current density of 1 A/g. The results in Fig. 8a demonstrate that samples have a small IR drop. The electrodes' C_{sp} was estimated from the discharge cycle using Eq. 11 [54, 55].

$$C_{sp} = \frac{I\,\Delta t}{m\,\Delta V} \tag{11}$$

where Δt is the discharge time, and ΔV is the potential range. Table 4 demonstrates the results and capacity enhancements for V_2O_5 samples after dopant addition, and capacitance increases with increasing dopant ratio owing to the higher SSA and larger V_p [56], which shortens the Li-ion route and speeds up Li^+ -ion diffusion [57]. These are consistent with what was gained from CV results.

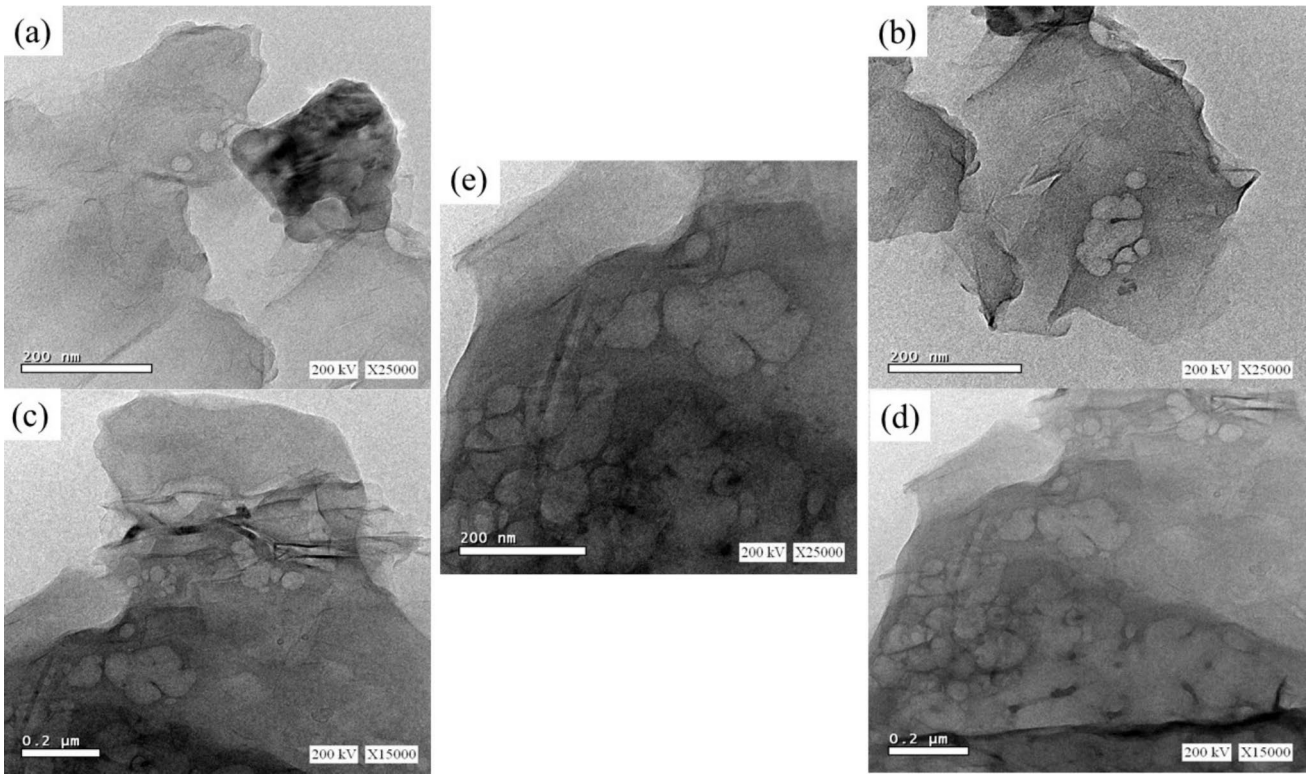

Fig. 5 TEM of **a**) pure, **b**) 1%, **c**) 2%, **d**) 3%, **e**) 4% Ti-doped V_2O_5

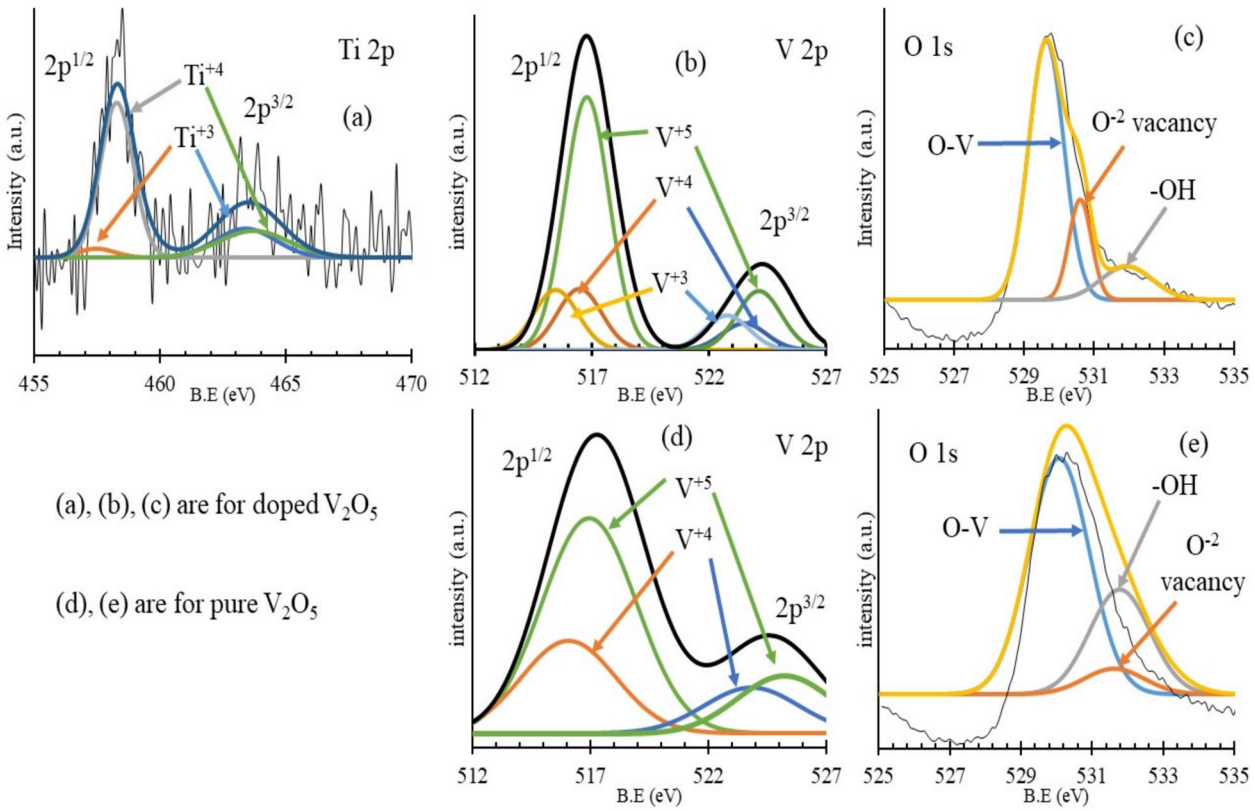

Fig. 6 XPS of pure and 4%Ti-V_2O_5

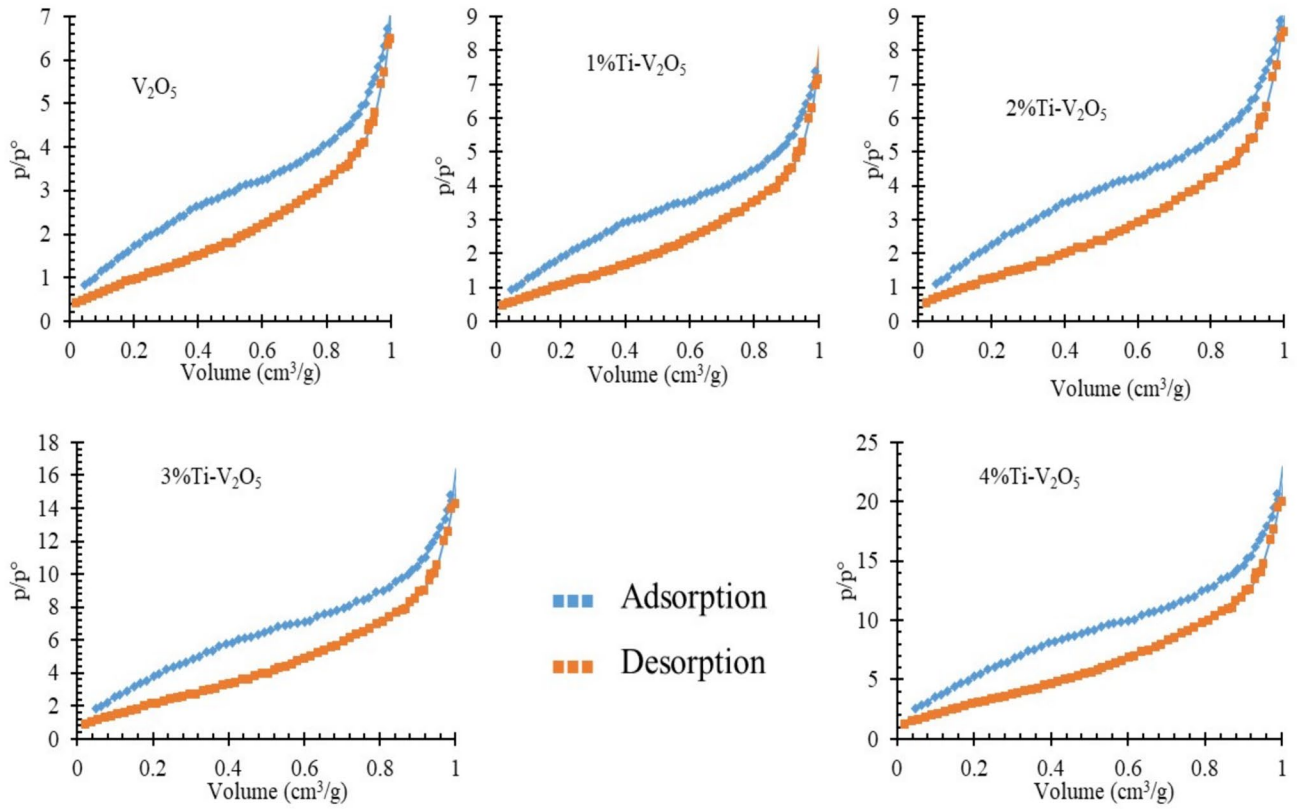

Fig. 7 BET of the prepared samples

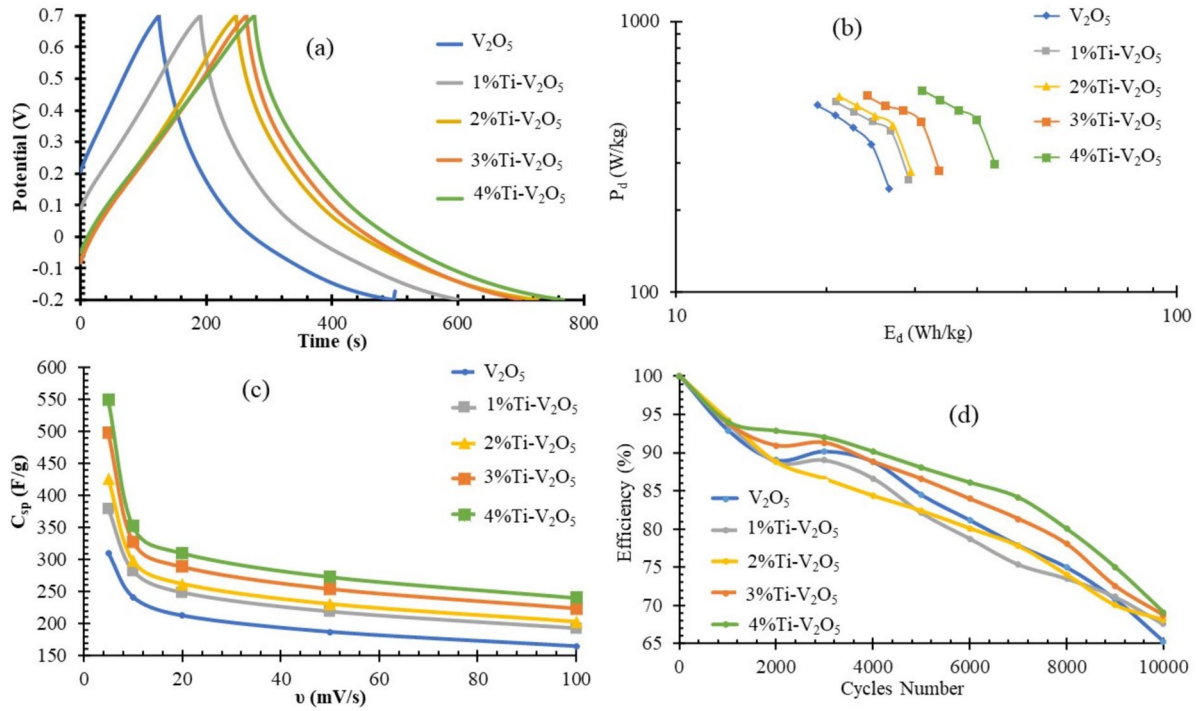

Fig. 8 Electrochemical studies of the prepared samples **a**) GCD at 1A/g, **b**) Ragone plot, **c**) capacitance-Scan rate relation, **d**) cycling stability for 10,000 cycles

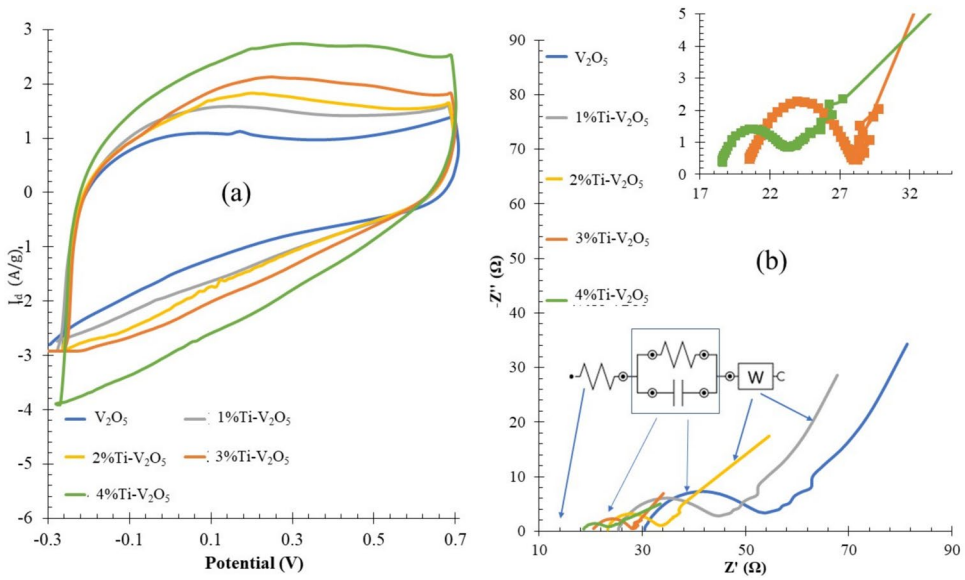

Fig. 9 Electrochemical studies of the prepared samples **a**) CV at 10 mV/s, **b**) EIS

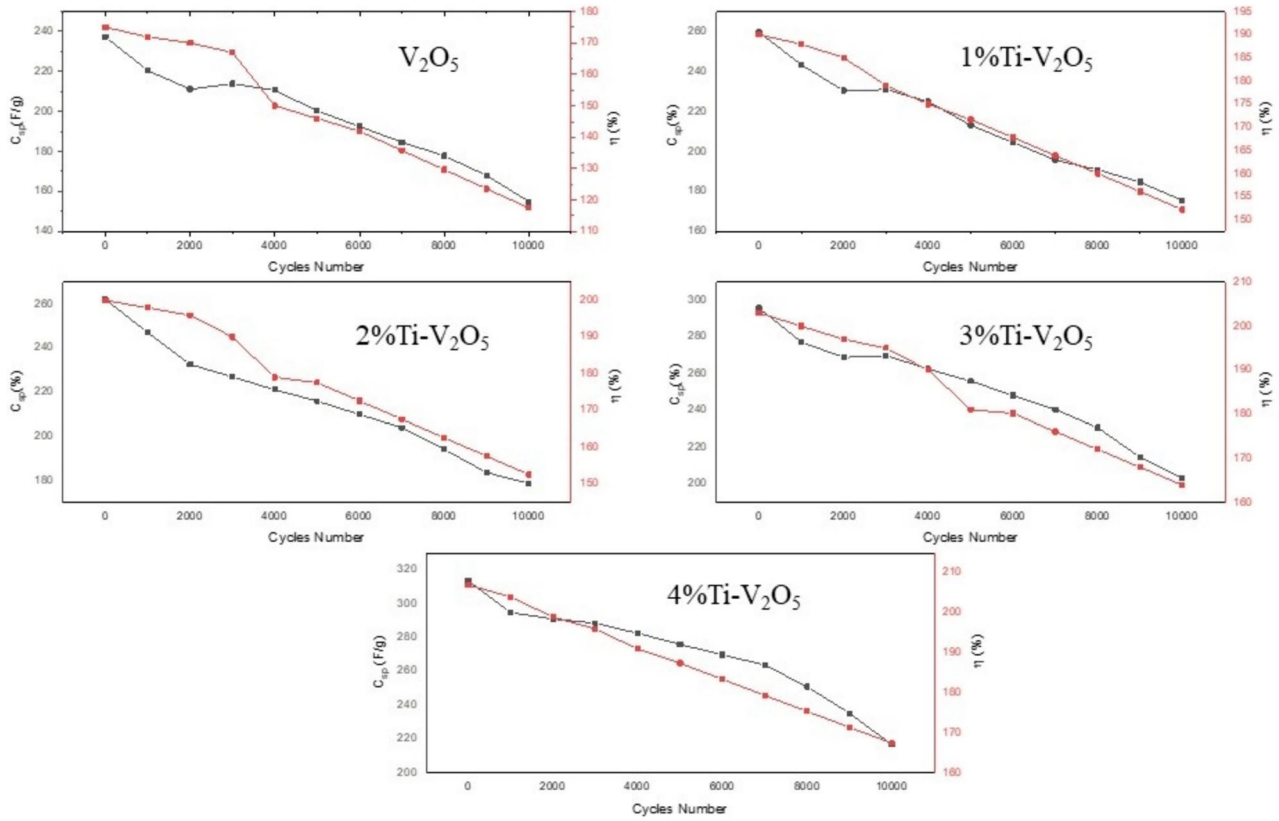

Fig. 10 C_{sp}/ η relation after 10,000 cycles for the prepraed samples

The energy density (E_d) and power density (P_d) are important parameters. They are calculated for the prepared V_2O_5 samples using Eqs. (12, 13) [58], and listed in Table 4

$$E_d = \frac{1}{2} C_{sp} \, \Delta V^2 \tag{12}$$

Table 4 Electrochemical capacitive data of the investigated materials

Sample	C_{sp} (F/g) 10 mV/s	C_{sp} (F/g) 1 A/g	At 0.2 V			Stability 10,000 cycles (%)	E_d (Wh/g)	P_d (W/kg)	C' (μF)	C'' (μF)	τ (ms)	R_S (Ω)	R_{ct} (Ω)
			b	k_1 (mA)	k_2 (mA)								
V_2O_5	254.6	237.4	0.53	0.8 ± 0.009	$0.02 \pm 3.4 \times 10^{-4}$	65.27	26.7	489.4	0.84	4.8	0.012	24	31
1%Ti-V_2O_5	282.2	259.7	0.57	1.1 ± 0.012	$0.05 \pm 4.2 \times 10^{-4}$	67.55	29.2	501.6	0.92	5.3	0.019	30	25
2%Ti-V_2O_5	297.8	262.2	0.64	1.7 ± 0.013	$0.1 \pm 9 \times 10^{-4}$	68.1	29.5	528.7	1.94	1.7	0.019	23	10
3%Ti-V_2O_5	328.1	295.8	0.67	1.8 ± 0.012	$0.11 \pm 8.2 \times 10^{-4}$	68.7	33.6	531.3	3.76	4.6	0.021	21	8
4%Ti-V_2O_5	352.3	313.6	0.71	1.8 ± 0.014	$0.11 \pm 7 \times 10^{-4}$	69.1	43.3	554.2	9.52	22	0.024	18	6

$$P_d = \frac{E_d}{t} \tag{13}$$

As shown in Fig. 8b, the Ragone plot of the prepared samples gives the supercapacitor behavior that shows an inverse relation (from the values of E_d and P_d at different current densities) [59].

For comparison with the previous studies, Table 5 shows the variation of morphology, dopants, and composing that affect the supercapacitive results.

For illustrating different capacitive mechanism types; CV is an appropriate technique. The prepared electrodes' CV was studied at 100, 50, 20, and 10 mV/s scanning rates. The redox peaks evident in the plots are caused by the redox of active sites at the electrodes. [65, 66].

Cyclic voltammetry (CV) of V_2O_5 electrodes in Fig. 9a show surface redox pseudocapacitive behavior [67] with a slight hump at + 0.2 V related to $V_2O_5 + xLi^+ + xe^- \leftrightarrow Li_xV_2O_5$ process, which as a result of Li hopping in the V_2O_5 crystal [68–70]. Doped V_2O_5 has a slightly shifted hump at + 0.19 V besides the formation of 2 humps at 0.24 V and 0.48 V, which are related to $VO^{2+} + H^+ + e^- \leftrightarrow VOH^{2+}$, and $2VO^+ + 2H_2O \leftrightarrow V_2O_4 + 4H^+ + 2e^-$ respectively [21]. The abundance of valence states of V^{+n} and VO^{+n} is related to adding Ti dopant that leads to $V_O^{\cdot\cdot}$ vacancy formation and enriching with dopant ratio increment. The multiple oxidation states of V, VO, and O^{-2} help for the presence of surface redox pseudocapacitive behavior of samples. Using Eq. (11), the specific capacitance (C_{sp}) values of electrodes under investigation from CV were calculated [71] and given in Table 4.

$$C_{sp} = \frac{1}{m\nu\Delta V}\int_{-V}^{+V} IV\partial V \tag{14}$$

where I is current, ΔV is applied potential, ν is scan rate, and m is the active material's mass. As shown in Fig. 8c Specific capacitance is inversely proportional to scan rate, and the result is convenient with Eq. 14. For a deeper analysis of the capacitive behavior, the b_O value was determined using a power law using Eq. (15) [72, 73]

$$I_m = a_o v^{bo} \tag{15}$$

where I_m is the maximum current density in CV plots, and a_o and b_o are constant parameters. Equation 8 states that the b_O value generally equals 1.0 for non-diffusion-controlled surface capacitive and 0.5 for diffusion-controlled redox reaction [74]. As listed in Table 4, b_O value of pure V_2O_5 indicates the battery type. On the other hand, b_o values of doped samples show that the hybrid system performs the battery-supercapacitor hybrid mechanism [75]. For further

Table 5 Comparison study of V_2O_5's previous results

Composite	Electrolyte	Cycle retention (%)	C_{sp}	Ref
V_2O_5 nanorods	0.5 M H_2SO_4	83% after 5000 cycles	4.17 F /cm^2	[59]
Ti-V_2O_5	1 M $LiClO_4$/ PC	119% after 2000 cycles	641 F/g	[60]
Mn-V_2O_5	1 M $LiPF_6$ in (EC)/ (EMC)	80% after 50 cycles	253 mAh/g	[61]
V_2O_5/MWCNTs	2 M $LiClO_4$	93% after 4000 cycles	160.1 F/g	[62]
V_2O_5	2 M KCl	76% after 600 cycles	316 F/g	[63]
Ti-V_2O_5/MWCNTs	1 M H_2SO_4	~113% after 400 cycles	310 F/g	[64]
Ti-V_2O_5	1 M $LiNO_3$	69.1% after 10,000 cycles	352.3 F/g	Present work

analysis, the following equation for current at a specific V is in Eq. 16 [76].

$$I(V) = k_1 v^{1/2} + k_2 v \tag{16}$$

Solving for k_1 and k_2 at each potential allows for separating the diffusion and capacitive currents, respectively. It's noticed from the k_1 and k_2 values in Table 4 that the charge tends to be higher for both diffusive and capacitive currents, owing to the increment of c-spacing with dopant addition that eases both diffusive and capacitive currents [77].

The Nyquist graphs for the investigated electrodes over the 10^{-2}-10^5 Hz frequency range are shown in Fig. 9b. Crossings of the Nyquist diagram on the Z'-axis at higher frequencies indicate the solution resistance. (R_s). In the high-frequency section, one depressed semicircle was generated by the charge transfer resistance (R_{ct}) at the electrode/electrolyte interface, which is related to the surface property of the electrode [78]. A spike at the lower frequencies was present, which suggested supercapacitor behavior called Warburg impedance (W) [78], also referred to as the diffusive resistance of Li^+ ions into the electrode. The semicircle that appeared at higher frequencies has been enlarged to better comprehend the charge transfer mechanism at electrolyte–electrode contact [79].

As listed in Table 4, adding the dopant leads to decreased R_{ct}, which decreases with an increasing dopant ratio. This may relate to multiple oxidations of V, Ti, and enriching the O^{-2} that ease the Li^+ ion diffusion.

The time constant (τ) of prepared electrodes was derived from angular frequency (ω) coordinated at the top of the semicircle using Eq. 17 [44]

$$\tau = \frac{1}{\omega} \tag{17}$$

Results are listed in Table 4, demonstrating the τ increment with dopant ratio increment, the remarkable power response sample shown by its small-time constants [80].

At a current density of 1 A/g, the electrochemical stability of examined electrodes was studied. The results are presented in Fig. 8d. They are summarised in Table 4, which demonstrates that the stability of the electrodes hasn't altered after 10000 cycles with a significant value (4.6%) between the highest value (4%Ti-V_2O_5) and lowest value (V_2O_5) of 65–70% of their initial capacitances.

For further explanation of the cyclic retention after 10,000 cycles, Fig. 10 shows a binary relation of C_{sp}, and η (coulmbic efficiency) to obtain further illustaration of electrodes' performance. η was calculated through the following equation [58]

$$\eta = {}^{t_d}/_{t_c} \times 100 \tag{18}$$

where t_d is discharge time, and t_c is charge time.

Conclusions

In conclusion, the electrochemical properties of pure and doped V_2O_5 sol–gel films in a 1 M $LiNO_3$ electrolyte were examined to identify their potential as an electrode for energy storage. The electrochemical process was tested through GCD, EIS, and CV techniques. The difference in dopant ratio showed a pronounced effect on the samples' electrochemical properties. All the tested electrodes showed surface redox pseudocapacitive behavior. The best performance was achieved for 4%Ti-V_2O_5, with the highest specific capacitance value of 313.6 F/g at 1 A/g. It also showed high performance of 89.6% for 1000 cycles 43.4 Wh/kg maximum energy density and 554.2 W/kg power density. The high performance of samples relies on incrementing the c lattice constant and $V_O^{\cdot\cdot}$ vacancy that help for both capacitive and diffusive charge storage. The results show the possibility of using Ti-doped V_2O_5 as electrodes for relatively cheap energy storage devices.

Acknowledgements I would like to express my deepest gratitude to Prof. Mahmoud Ahmed Mousa. Prof. of Physical Chemistry, Faculty of Science, Benha University, Egypt for his permanent limitless support.

References

1. Kumar S, Saeed G, Zhu L, Hui KN, Kim NH, Lee JH (2021) (2020) 0D to 3D carbon-based networks combined with pseudocapacitive electrode material for high energy density supercapacitor: A review. Chem Eng J 403(May 2020):126352. https://doi.org/10.1016/j.cej.2020.126352
2. Liu S, Ni D, Li HF, Hui KN, Ouyang CY, Jun SC (2018) Effect of cation substitution on the pseudocapacitive performance of spinel cobaltite MCo2O4 (M = Mn, Ni, Cu, and Co). J Mater Chem A 6(23):10674–10685. https://doi.org/10.1039/c8ta00540k
3. Liu H et al (2024) Marangoni-driven self-assembly MXene as functional membrane enables dendrite-free and flexible zinc–Iodine pouch cells. Adv Energ Mater 14:2400318. https://doi.org/10.1002/aenm.202400318
4. Liu H et al (2024) Polyhydroxylated Organic Molecular Additives for Durable Aqueous Zinc Battery. Adv Funct Mater 34:2309840
5. Liu H, Hu L, Soomro RA, Xu B (2023) Organic salt-derived phosphorus-doped mesoporous carbon for high performance supercapacitors. Chinese Chem Lett 34(8):108004. https://doi.org/10.1016/j.cclet.2022.108004
6. Cao B et al (2024) Biomass-derived carbon-sulfur hybrids boosting electrochemical kinetics to achieve high potassium storage performance. J Colloid Interface Sci 661(January):598–605. https://doi.org/10.1016/j.jcis.2024.01.201
7. Zhang S et al (2020) Large-scale preparation of solution-processable one-dimensional V2O5 nanobelts with ultrahigh aspect ratio for bifunctional multicolor electrochromic and supercapacitor applications. J Alloys Compd 842:155882. https://doi.org/10.1016/j.jallcom.2020.155882
8. Zeng HM, Zhao Y, Hao YJ, Lai QY, Huang JH, Ji XY (2009) Preparation and capacitive properties of sheet V6O13 for electrochemical supercapacitor. J Alloys Compd 477(1–2):800–804. https://doi.org/10.1016/j.jallcom.2008.10.100
9. Zhang J, Zhang H, Liu M, Xu Q, Jiang H, Li C (2020) Cobalt-stabilized oxygen vacancy of V2O5 nanosheet arrays with delocalized valence electron for alkaline water splitting. Chem Eng Sci 227:115915. https://doi.org/10.1016/j.ces.2020.115915
10. Song H, Zhang C, Liu Y, Liu C, Nan X, Cao G (2015) Facile synthesis of mesoporous V2O5 nanosheets with superior rate capability and excellent cycling stability for lithium ion batteries. J Power Sources 294:1–7. https://doi.org/10.1016/j.jpowsour.2015.06.055
11. Pradeeswari K et al (2020) Effect of cerium on electrochemical properties of V2O5 nanoparticles synthesized via non-aqueous sol-gel technique. Ionics (Kiel) 26(2):905–912. https://doi.org/10.1007/s11581-019-03259-z
12. Zhang Y et al (2020) Constructing defect-rich V2O5 nanorods in catalytic membrane electrode for highly efficient oxidation of cyclohexane. J Catal 387:154–162. https://doi.org/10.1016/j.jcat.2020.04.023
13. Xiao ZR, Guo GY (2009) Structural, electronic and magnetic properties of V2O5-x: an ab initio study. J Chem Phys 130(21):214704. https://doi.org/10.1063/1.3146790.
14. Semenenko DA et al (2010) Electrochemistry Communications LixV2O5 nanobelts for high capacity lithium-ion battery cathodes. Electrochem Commun 12(9):1154–1157
15. Zu D et al (2019) Oxygen-deficient metal oxides: Synthesis routes and applications in energy and environment. Nano Res 12(9):2150–2163. https://doi.org/10.1007/s12274-019-2377-9
16. Yao X, Guo G, Li PZ, Luo ZZ, Yan Q, Zhao Y (2017) Scalable Synthesis of Honeycomblike V2O5/Carbon Nanotube Networks as Enhanced Cathodes for Lithium-Ion Batteries. ACS Appl Mater Interfaces 9(49):42438–42443. https://doi.org/10.1021/acsami.7b15136
17. Li L, Hui KS, Hui KN, Cho YR (2017) Ultrathin petal-like NiAl layered double oxide/sulfide composites as an advanced electrode for high-performance asymmetric supercapacitors. J Mater Chem A 5(37):19687–19696. https://doi.org/10.1039/c7ta06119f
18. Zhu J et al (2013) Building 3D Structures of Vanadium Pentoxide Nanosheets and Application as Electrodes in Supercapacitors. Nano Lett 13(10–11):5408–5413. https://doi.org/10.3109/10641968409046134
19. Ngamwongwan L, Fongkaew I, Jungthawan S, Hirunsit P, Limpijumnong S, Suthirakun S (2021) Electronic and thermodynamic properties of native point defects in V2O5: a first-principles study. Phys Chem Chem Phys 23(19):11374–11387. https://doi.org/10.1039/d0cp06002j
20. Bi W et al (2019) V2O5-Conductive polymer nanocables with built-in local electric field derived from interfacial oxygen vacancies for high energy density supercapacitors. J Mater Chem A 7(30):17966–17973. https://doi.org/10.1039/c9ta04264d
21. Zhang X, Liu X, Zeng Y, Tong Y, Lu X (2020) Oxygen Defects in Promoting the Electrochemical Performance of Metal Oxides for Supercapacitors: Recent Advances and Challenges. Small Methods 4(6):1–18. https://doi.org/10.1002/smtd.201900823
22. Salek G, Bellanger B, Mjejri I, Gaudon M, Rougier A (2016) Polyol Synthesis of Ti-V2O5 Nanoparticles and Their Use as Electrochromic Films. Inorg Chem 55(19):9838–9847. https://doi.org/10.1021/acs.inorgchem.6b01662
23. Liu H, He H, Chen L, Pan Q, Zhang G (2021) Flower-like Co3O4 sensor with rich oxygen vacancy defects for enhancing room temperature NOx sensing performances. J Alloys Compd 868:159180. https://doi.org/10.1016/j.jallcom.2021.159180
24. Le TK, Kang M, Tran VT, Kim SW (2019) Relation of photoluminescence and sunlight photocatalytic activities of pure V2O5 nanohollows and V2O5/RGO nanocomposites. Mater Sci Semicond Process 100(March):159–166. https://doi.org/10.1016/j.mssp.2019.04.047
25. Ma H et al (2021) Speed enhancement of ultraviolet photodetector base on ZnO quantum dots by oxygen adsorption on surface defects. J Alloys Compd 868:159252. https://doi.org/10.1016/j.jallcom.2021.159252
26. Tepavcevic S et al (2012) Nanostructured bilayered vanadium oxide electrodes for rechargeable sodium-ion batteries. ACS Nano 6(1):530–538. https://doi.org/10.1021/nn203869a
27. Abdelrazek MM, Hannora AE, Kamel RM, Morad I, El-Desoky MM (2023) Effect of lanthanum doping on the structure and optical properties of nanocrystalline vanadium pentoxide films prepared by sol-gel method effect of lanthanum doping on the structure and optical properties of nanocrystalline vanadium pentoxide films prepar. Opt Quantum Electron 55:491. https://doi.org/10.1007/s11082-023-04764-2
28. Zhu S et al (2022) Vanadium pentoxide nanosheets with rich oxygen vacancies as a high-performance electrode for supercapacitors. Ionics (Kiel) 28(6):2931–2942. https://doi.org/10.1007/s11581-022-04541-3
29. Jia YQ (1991) Crystal radii and effective ionic radii of the rare earth ions. J Solid State Chem 95(1):184–187. https://doi.org/10.1016/0022-4596(91)90388-X
30. Shannon RD (1976) Revised Effective Ionic Radii and Systematic Studies of Interatomie Distances in Halides and Chaleogenides. Acta Crystallogr 32:751. https://doi.org/10.1023/A:1018927109487
31. Durmus Z, Baykal A, Kavas H, Szeri H (2011) Preparation and characterization of polyaniline (PANI)-Mn3O4 nanocomposite. Phys B Condens Matter 406(5):1114–1120. https://doi.org/10.1016/j.physb.2010.12.059
32. Lee B, Yoon JR (2013) Preparation and characteristics of Li4Ti5O12 with various dopants as anode electrode for hybrid

supercapacitor. Curr Appl Phys 13(7):1350–1353. https://doi.org/10.1016/j.cap.2013.04.002
33. Qasim KF, Mousa MA (2023) Physicochemical Properties of Oriented Crystalline Assembled Polyaniline/Metal Doped Li4Ti5O12 Composites for Li-ion Storage. J Inorg Organomet Polym Mater 33(9):2601–2617. https://doi.org/10.1007/s10904-023-02720-x
34. Ahmed N, Ramadan M, El WMA (2018) Non-precious co-catalysts boost the performance of TiO2 hierarchical hollow mesoporous spheres in solar fuel cells. Int J Hydrogen Energy 43(October):21219–21230. https://doi.org/10.1016/j.ijhydene.2018.10.012
35. Mohamed SK, Bashat AMA, Hassan HMA, Ismail N, El Rouby WMA (2023) Optimizing the performance of Auy/Nix/TiO2NTs photoanodes for photoelectrochemical water splitting. RSC Adv 13(20):14018–14032. https://doi.org/10.1039/d3ra02011h
36. Wang J, Zhou Y, Liao T, Lin Z (2007) Trend in crystal structure of layered ternary T-Al-C carbides T = Sc, Ti, V, Cr, Zr, Nb, Mo, Hf, W and Ta). J Mater Res 22(10):2685–2690. https://doi.org/10.1557/jmr.2007.0366
37. Heryanto B, Abdullah D (2019) Tahir, and Mahdalia, "Quantitative analysis of X-Ray diffraction spectra for determine structural properties and deformation energy of Al, Cu and Si." J Phys Conf Ser 1317(1):012052. https://doi.org/10.1088/1742-6596/1317/1/012052
38. Kommu P, Singh GP, Chakra CS, Jana S, Kumar V, Bhattacharyya AS (2020) Preparation of ZnMn2O4 and ZnMn2O4/graphene nano composites by combustion synthesis for their electrochemical properties. Mater Sci Eng B Solid-State Mater Adv Technol 261:114647. https://doi.org/10.1016/j.mseb.2020.114647
39. Gunkel F, Christensen DV, Chen YZ, Pryds N (2020) Oxygen vacancies: the (in)visible friend of oxide electronics. Appl Phys Lett 116(12):120505. https://doi.org/10.1063/1.5143309
40. Guilhaume N, Primet M (1994) Catalytic combustion of methane: Copper oxide supported on high-specific-area spinels synthesized by a sol-gel process. J Chem Soc Faraday Trans 90(11):1541–1545. https://doi.org/10.1039/FT9949001541
41. Osonkie A, Lee V, Chukwunenye P, Cundari T, Kelber J (2020) Plasma modification of vanadium oxynitride surfaces: characterization by in situ XPS experiments and DFT calculations. J Chem Phys 153(14)144709. https://doi.org/10.1063/5.0027996
42. Hryha E, Rutqvist E, Nyborg L (2012) Stoichiometric vanadium oxides studied by XPS. Surf Interface Anal 44(8):1022–1025. https://doi.org/10.1002/sia.3844
43. Silversmit G, Depla D, Poelman H, Marin GB, De Gryse R (2006) An XPS study on the surface reduction of V2O5 (001) induced by Ar+ ion bombardment. Surf Sci 600:3512–3517. https://doi.org/10.1016/j.susc.2006.07.006
44. Silversmit G, Depla D, Poelman H, Marin GB, De Gryse R (2004) Determination of the V2p XPS binding energies for different vanadium oxidation states (V5+ to V0+). J Electron Spectros Relat Phenomena 135:167–175. https://doi.org/10.1016/j.elspec.2004.03.004
45. Mendialdua J, Casanova R, Barbaux Y (1995) XPS studies of V2O5, V6O13, VO2 and V2O3. J Electron Spectros Relat Phenomena 71:249–261
46. Bharti B, Kumar S, Lee HN, Kumar R (2016) Formation of oxygen vacancies and Ti3+ state in TiO2 thin film and enhanced optical properties by air plasma treatment. Sci Rep 6(May):1–12. https://doi.org/10.1038/srep32355
47. Akkinepally B, Reddy IN, Lee C, Jo T, Rao PS, Shim J (2023) Promising electrode material of Fe3O4 nanoparticles decorated on V2O5 nanobelts for high-performance symmetric supercapacitors. Ceram Int 49(4):6280–6288. https://doi.org/10.1016/j.ceramint.2022.10.161
48. Haetge J, Hartmann P, Brezesinski K, Janek J, Brezesinski T (2011) Ordered Large-Pore Mesoporous Li4Ti5O12 Spinel Thin Film Electrodes with Nanocrystalline Framework for High Rate Rechargeable Lithium Batteries: Relationships among Charge Storage, Electrical Conductivity, and Nanoscale Structure. Chem Mater 23(19):4384–4393. https://doi.org/10.1021/cm202185y
49. Kamar EA, Qasim KF, Mousa MA (2022) Supercapacitor and oxygen evolution reaction performances based on rGO and Mn2V2O7 nanomaterials. Electrochim Acta 430:141106. https://doi.org/10.1016/j.electacta.2022.141106
50. Zhao H et al (2013) Effects of oxygen vacancy on the electronic structure and multiferroics in sol-gel derived Pb0.8Co0.2TiO3 thin films. Dalt Trans 42(28):10358–10364. https://doi.org/10.1039/c3dt50257k
51. Paparazzo E (2021) XPS quantification of oxygen vacancies in mesoporous and non-mesoporous CeO2: Comment on an article by Thill: et al. J. Mater. Chem. A, 2020, 8, 24752–24762. J Mater Chem A 9(41):23722–23725. https://doi.org/10.1039/d1ta00387a
52. Wang Z, Wang L (2021) Role of oxygen vacancy in metal oxide based photoelectrochemical water splitting. EcoMat 3(1):1–13. https://doi.org/10.1002/eom2.12075
53. Hassan HMA et al (2023) Controllable fabrication of Zn2+ self-doped TiO2 tubular nanocomposite for highly efficient water treatment. Molecules 28(7):3072. https://doi.org/10.3390/molecules28073072
54. Qasim KF, Bayoumy WA, Mousa MA (2020) Electrical and electrochemical studies of core–shell structured nanorods of LiMn2O4@PANI composite. J Mater Sci Mater Electron 31:19526–19540. https://doi.org/10.1007/s10854-020-04482-5
55. Sri B, Akkinepally B, Shim J, Lim J (2024) Hybrid NiO@TiO2 nano-architecture for improved electrochemical performance with simulation corroboration. J Energy Storage 87(December 2023):111466. https://doi.org/10.1016/j.est.2024.111466
56. Mohamed SK, Elsalam SA, Shahat A, Hassan HMA, Kamel RM (2021) Efficient sucrose-derived mesoporous carbon sphere electrodes with enhanced hydrophilicity for water capacitive deionization at low cell voltages. New J Chem 45(4):1904–1914. https://doi.org/10.1039/d0nj05412g
57. Khairy M, Bayoumy WA, Faisal K, Elshereafy EE, Mousa MA (2020) Electrical and Electrochemical Behavior of Binary Li4Ti5O12–Polyaniline Composite. J Inorg Organomet Polym Mater 30(8):3158–3169. https://doi.org/10.1007/s10904-020-01478-w
58. Qasim KF, Mousa MA (2022) Effect of Oxidizer on PANI for Producing BaTiO3@PANI Perovskite Composites and Their Electrical and Electrochemical Properties. J Inorg Organomet Polym Mater 32(8):3093–3105. https://doi.org/10.1007/s10904-022-02335-8
59. Basu R, Ghosh S, Bera S, Das A, Dhara S (2019) Phase-pure VO 2 nanoporous structure for binder-free supercapacitor performances. Sci Rep 9(1):1–11. https://doi.org/10.1038/s41598-019-40225-1
60. Zheng J, Zhang Y, Hu T, Lv T, Meng C (2018) New Strategy for the Morphology-Controlled Synthesis of V2O5 Microcrystals with Enhanced Capacitance as Battery-type Supercapacitor Electrodes. Cryst Growth Des 18(9):5365–5376. https://doi.org/10.1021/acs.cgd.8b00776
61. Zeng H et al (2015) Nanostructured Mn-Doped V2O5 Cathode Material Fabricated from Layered Vanadium Jarosite. Chem Mater 27(21):7331–7336. https://doi.org/10.1021/acs.chemmater.5b02840
62. Pandit B, Dubal DP, Gómez-Romero P, Kale BB, Sankapal BR (2017) V2O5 encapsulated MWCNTs in 2D surface architecture: Complete solid-state bendable highly stabilized energy efficient

supercapacitor device. Sci Rep 7(2016):1–12. https://doi.org/10.1038/srep43430
63. Saravanakumar B, Purushothaman KK, Muralidharan G (2012) Interconnected V2O5 nanoporous network for high-performance supercapacitors. ACS Appl Mater Interfaces 4(9):4484–4490. https://doi.org/10.1021/am301162p
64. Jampani PH et al (2015) High energy density titanium doped-vanadium oxide-vertically aligned CNT composite electrodes for supercapacitor applications. J Mater Chem A 3(16):8413–8432. https://doi.org/10.1039/c4ta06777k
65. Yang ZY et al (2014) Controllable growth of CNTs on graphene as high-performance electrode material for supercapacitors. ACS Appl Mater Interfaces 6(11):8497–8504. https://doi.org/10.1021/am501362g
66. Shiquan Hong ZG, Huang X, Liu H (2019) In Situ chemical synthesis of MnO2/HMCNT nanocomposite with a uniquely developed three-dimensional open porous architecture for supercapacitors. J Inorg Organomet Polym Mater 29:1587–15960
67. Gogotsi Y, Penner RM (2018) Energy Storage in Nanomaterials - Capacitive, Pseudocapacitive, or Battery-like? ACS Nano 12(3):2081–2083. https://doi.org/10.1021/acsnano.8b01914
68. Wilkening M, Amade R, Iwaniak W, Heitjans P (2007) Ultraslow Li diffusion in spinel-type structured Li4Ti5O12- A comparison of results from solid state NMR and impedance spectroscopy. Phys Chem Chem Phys 9(10):1239–1246. https://doi.org/10.1039/b616269j
69. Pu X et al (2021) Understanding and calibration of charge storage mechanism in cyclic voltammetry curves. Angew Chemie - Int Ed 60(39):21310–21318. https://doi.org/10.1002/anie.202104167
70. Zaghib K, Simoneau M, Armand M, Gauthier M (1999) Electrochemical study of Li4Ti5O12 as negative electrode for Li-ion polymer rechargeable batteries. J Power Sources 81–82:300–305. https://doi.org/10.1016/S0378-7753(99)00209-8
71. Ciszewski M, Mianowski A, Szatkowski P, Nawrat G, Adamek J (2014) Reduced graphene oxide–bismuth oxide composite as electrode material for supercapacitors. Ionics (Kiel) 21(2):557–563. https://doi.org/10.1007/s11581-014-1182-4
72. Kalasina S et al (2018) Novel Hybrid Energy Conversion and Storage Cell with Photovoltaic and Supercapacitor Effects in Ionic Liquid Electrolyte. Sci Rep 8(1):1–11. https://doi.org/10.1038/s41598-018-30707-z
73. Akkinepally B, Robin N, Reddy IN, Rao HJ, Sooppy K, Shim J (2024) Unlocking enhanced electrochemical performance of SnO2-Bi2WO6 nanoflowers for advanced supercapacitor device. J Alloys Compd 970(October 2023):172677. https://doi.org/10.1016/j.jallcom.2023.172677
74. Etman AE, Ibrahim AM, Darwish FAM, Qasim KF (2023) A 10 years-developmental study on conducting polymers composites for supercapacitors electrodes : A review for extensive data interpretation. J Ind Eng Chem 122:27–45. https://doi.org/10.1016/j.jiec.2023.03.008
75. Shao Y et al (2018) Design and Mechanisms of Asymmetric Supercapacitors. Chem Rev 118(18):9233–9280. https://doi.org/10.1021/acs.chemrev.8b00252
76. Henrik L, So S, Solbrand A, Hjelm J, Hagfeldt A, Lindquist S (1997) Li Ion insertion in TiO2(Anatase), voltammetry on nanoporous films.pdf. J Phys Chem B 2(97):7717–7722
77. Faisal K, Abdelhamed S, Elaraby A, Ahmed M (2024) Polyaniline impact on graphitic C3N4's structural and physicochemical properties for high stability energy storage systems : Practical and theoretical studies. J Ind Eng Chem 139:325–335. https://doi.org/10.1016/j.jiec.2024.05.011
78. Rajalakshmi R, Remya KP, Viswanathan C, Ponpandian N (2021) Enhanced electrochemical activities of morphologically tuned MnFe2O4 nanoneedles and nanoparticles integrated on reduced graphene oxide for highly efficient supercapacitor electrodes. Nanoscale Adv 3(10):2887–2901. https://doi.org/10.1039/d1na00144b
79. Javed MS, Lei H, Wang Z, Tian Liu B, Cai X, Mai W (2020) 2D V2O5 nanosheets as a binder-free high-energy cathode for ultrafast aqueous and flexible Zn-ion batteries. Nano Energy 70(January):104573. https://doi.org/10.1016/j.nanoen.2020.104573
80. Qasim KF, Mousa MA (2021) Electrical and dielectric properties of self-assembled polyaniline on barium sulphate surface. Egypt J Pet 30(4):9–19. https://doi.org/10.1016/j.ejpe.2021.09.001

Publisher's Note Springer Nature remains neutral with regard to jurisdictional claims in published maps and institutional affiliations.

Springer Nature or its licensor (e.g. a society or other partner) holds exclusive rights to this article under a publishing agreement with the author(s) or other rightsholder(s); author self-archiving of the accepted manuscript version of this article is solely governed by the terms of such publishing agreement and applicable law.